Chemical Science

ROYAL SOCIETY OF CHEMISTRY

EDGE ARTICLE

View Article Online
View Journal

Check for updates

Cite this: DOI: 10.1039/d4sc01780c

Received 16th March 2024
Accepted 11th May 2024

DOI: 10.1039/d4sc01780c

rsc.li/chemical-science

Identification of two-dimensional covalent organic frameworks with mcm topology and their application in photocatalytic hydrogen evolution†

Peng-Ju Tian,‡ Xiang-Hao Han,‡ Qiao-Yan Qi and Xin Zhao *

Covalent organic frameworks have attracted considerable attention in recent years as a distinct class of crystalline porous organic materials. Their functional properties are inherently linked to their structural characteristics. Although hundreds of COFs have been reported so far, the types of their topologic structure are still limited. In this article, we report the identification of **mcm** topology for three porphyrin-based two-dimensional COFs, which are constructed from [4 + 4] imine condensation reactions. The **mcm** net is generated by pentagonal tiling, which has not been identified for COFs before. The structure of the COFs is elucidated by a variety of experimental characterization and structural simulations, by which their reticular frameworks exclusively composed of pentagonal pores have been confirmed. Moreover, the COFs exhibit high performance in photocatalytic hydrogen evolution from water, with the best one up to 10.0 mmol g^{-1} h^{-1} after depositing 0.76 wt% Pt as a co-catalyst. This study identifies **mcm** topology for COFs for the first time and highlights the potential of these COFs as promising photocatalysts for sustainable hydrogen production from water.

Introduction

Covalent organic frameworks (COFs) represent a class of crystalline porous organic polymers constructed *via* interconnecting organic building blocks with covalent bonds, guided by the principle of reticular chemistry.[1–3] The physical and chemical properties of COFs are significantly influenced by their network structures, which are mainly classified into two categories: two-dimensional (2D) and three dimensional (3D) frameworks according to the spatial extension of interconnections of building blocks.[4–7] The combination of building blocks with different symmetries may lead to the formation of COFs with various topologies, from which different shapes of pores can be generated. Currently more than 20 topologies have been experimentally realized for 3D COFs.[8–10] However, as far as the types of 2D COFs are concerned, to the best of our knowledge, so far only 13 topologies, including **hcb**,[11] **hxl**,[12] **sql**,[13] **kgm**,[14] **kgd**,[15] **tth**,[16] **mtf**,[17] **bex**,[18] **fxt**,[19] **cpi**,[20] **htb**,[21] **cem**,[22] and **tju**[23] nets, have been identified or proposed for the COFs reported in the literature. Among these topologies, most of the pore shapes are triangular, quadrangular, or hexagonal.[11–19,21–23] Surprisingly, pentagonal pores are rarely observed in COFs and currently only the **cpi** net includes pentagonal faces but they are tiled with hexagonal faces.[20] COFs with **mcm** topology, that is, those that are composed of only pentagonal pores, have not been identified yet, although such a topology has already been theoretically proposed for COFs and predicted to exhibit unique properties.[24,25] The difficulty in the construction of such a type of COF could be attributed to the nonedge-transitive feature of **mcm** topology, for which both the angles and lengths of its building blocks need to match each other.[16] This requirement poses a challenge to the design and construction of this kind of COF.

As a class of functional porous materials, COFs have exhibited great application potential in diverse fields, including gas storage/separation,[26–30] heterogeneous catalysis,[31–33] energy storage,[34–37] sensors,[38,39] optoelectronics,[40–43] and so on. Among them, COFs as photocatalysts for the hydrogen evolution reaction (HER) from water have drawn considerable attention in recent years because of their structural advantages, such as high crystallinity, designable structure, highly accessible surface areas, abundant photo-active sites, and efficient transport of photogenerated charges.[44] Since Lotsch and co-workers reported the first example of applying a COF for the HER in 2014,[45] a variety of COFs have been developed for the photocatalytic HER and the efficiency of the photocatalysts has become higher and higher over the past several years.[46–48] However, to explore high performance photocatalysts for the HER, increasing their structure diversity is still urgent. Herein, we report the synthesis of three porphyrin-based 2D COFs. Their topology was identified as a **mcm** net based on structure elucidation. Moreover, their photocatalytic performance for

---

State Key Laboratory of Organometallic Chemistry, Shanghai Institute of Organic Chemistry, University of Chinese Academy of Sciences, Chinese Academy of Sciences, 345 Lingling Road, Shanghai 200032, China. E-mail: xzhao@sioc.ac.cn

† Electronic supplementary information (ESI) available. See DOI: https://doi.org/10.1039/d4sc01780c

‡ These authors contributed equally to this work.

hydrogen evolution from water was investigated, and a high catalytic efficiency was observed.

Results and discussion

The synthesis of the three COFs was performed through the Schiff-base reaction of C_4 symmetric tetraamine tetrakis(4-aminophenyl)porphyrin with different metal ions (TAPP-M) and D_{2h} symmetric tetraaldehyde 4,4′,4″,4‴-([1,1′-biphenyl]-4,4′-diylbis(azanetriyl))tetrabenzaldehyde (BATA) under solvothermal conditions (Scheme 1). The reaction conditions were optimized by screening various solvents and aqueous acetic acid solutions to afford the COFs as microcrystallites with high crystallinity. Specifically, COF-BATA-TAPP-H_2 was obtained as crystalline purple powder by heating the monomers in a mixture of mesitylene and *n*-butanol with 6 M aqueous acetic acid as a catalyst at 120 °C for 72 h, while COF-BATA-TAPP-Ni and COF-BATA-TAPP-Zn were synthesized by a similar method but with different organic solvents and different concentrations of aqueous acetic acid (see the ESI† for details). The Fourier transform infrared (FT-IR) spectra of these COFs showed a significant decrease in the intensity of the bands corresponding to C═O and N–H stretching vibrations (1695 and 3360 cm^{-1}, respectively) in comparison with those of the monomers BATA and TAPP (Fig. S1†). Meanwhile, the appearance of C═N stretching vibration at 1626 cm^{-1} in the FT-IR spectra of the three COFs indicated the successful polymerization and the consumption of the monomers. Moreover, the formation of C═N bonds in the polymers was also supported by the peaks with chemical shifts at ∼160 ppm in the solid-state ^{13}C cross-polarization magic angle spinning (CP/MAS) NMR spectra of the COFs (Fig. S2–S4†). In addition, X-ray photoelectron spectroscopy (XPS) measurements were carried out to evaluate the content and valence state of metals in COF-BATA-TAPP-M. The experimental values of metal content for the two COFs are 1.2 at%, which matched well with the theoretical values (Table S1†). The strong peaks in the XPS spectrum of COF-BATA-TAPP-Ni, which appeared at 855.46 eV and 872.69 eV, should be attributed to Ni $2p_{3/2}$ and Ni $2p_{1/2}$. The peaks that appeared at 1021.87 eV and 1044.88 eV in the XPS spectrum of COF-BATA-TAPP-Zn should be attributed to Zn $2p_{3/2}$ and Zn $2p_{1/2}$. These results indicated that the valence state of Ni and Zn in the COFs was +2 (Fig. S5–7†). The morphology of the COFs was observed with transmission electron microscopy (TEM). The recorded TEM images show that all three COFs exhibit a sheet-like morphology (Fig. S8–S10†), consistent with their 2D structures. Their thermal stability was investigated with thermogravimetric analysis. Their 5% weight loss was observed at 540, 504, and 448 °C for COF-BATA-TAPP-H_2, COF-BATA-TAPP-Ni, and COF-BATA-TAPP-Zn, respectively, indicating that they all have high thermal stability (Fig. S11†).

After the acquisition of the polymers, structural simulations and powder X-ray diffraction (PXRD) analysis were conducted to elucidate their crystal structures. In principle, two types of frameworks with **bex** topology and **mcm** topology, respectively, could be produced from the assembly of a cross-like C_4 symmetric building block (I) and a D_{2h} symmetric building block (II) (Fig. 1a). The difference in the spatial locations of the building blocks between the **bex** net and **mcm** net lies in the different arrangement of the building block II. In a COF with **bex** topology, the building block II adopts a parallel array. However, in a COF with **mcm** topology, the building block II is

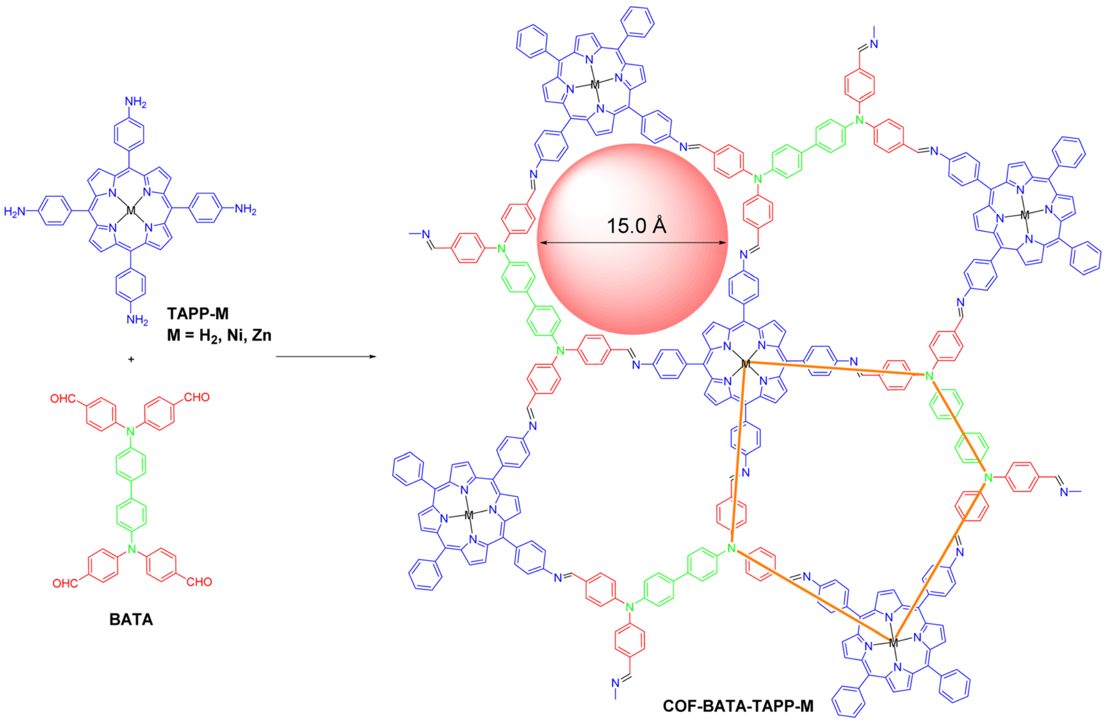

Scheme 1 Synthesis of COF-BATA-TAPP-M.

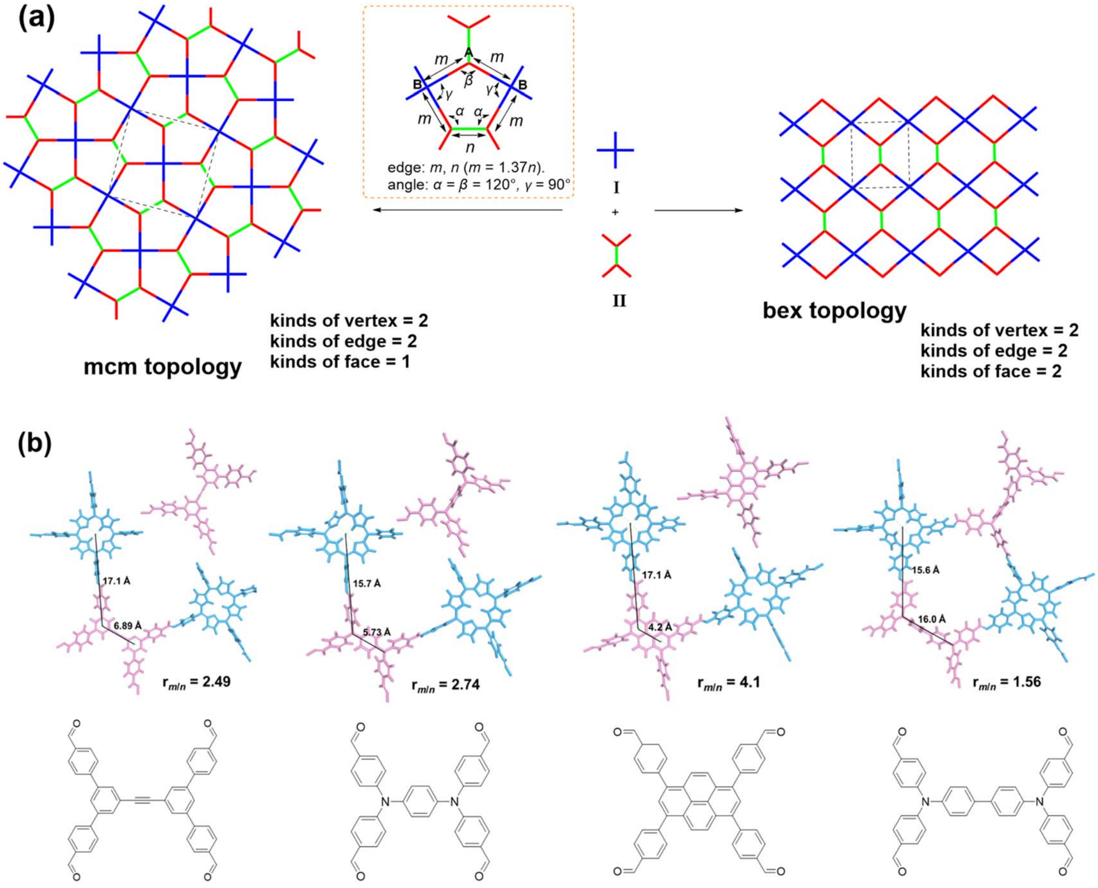

Fig. 1 (a) Illustration for the formation of COFs with **mcm** (left) and **bex** (right) topologies from the assembly of building blocks I and II, and the relationship between the vertex, edge, and angle in **mcm** topology (middle). (b) Illustration to show the length ratios of the edges to fit or unfit the formation of a COF with **mcm** topology.

arranged in a perpendicular position. It should be noted that structures with **bex** topology have been depicted for all the previously reported COFs constructed from the combination of these two kinds of building blocks,[49–59] including two COFs synthesized from the same monomers as the ones in this work but under different solvothermal conditions.[60,61] Indeed, most of the COFs in these previous studies should hold **bex** topology, not **mcm**, because the length ratio of their building blocks does not meet the requirement for the formation of the **mcm** net, which is explained as follows. As shown in Fig. 1a, the **mcm** net has 2 kinds of vertex (A and B), 2 kinds of edge (m and n), 3 kinds of corner (α, β, and γ), and one kind of face. The connection number of vertex A is 3 and the connection number of vertex B is 4. According to the structure of vertex B, the angle of γ should be 90°. For the angles of α and β, they can vary but need to keep $2\alpha + \beta = 360°$. To favor the design of building blocks in COFs, both the angles of α and β are fixed to 120°, because organic molecules with such a structure are readily synthesized. For this design, the as-proposed pentagon pore has three 120° corners and two 90° corners, with four edge m and one edge n. On the basis of the geometry of this structure, the length ratio of edge m and edge n ($r_{m/n}$) is calculated to be 1.37. Therefore, to construct a **mcm** net, the building blocks must be judiciously selected to make $r_{m/n}$ equal or close to 1.37. The values of $r_{m/n}$ of some building blocks were calculated and are shown in Fig. 1b. The results show that the former three cannot form COFs with **mcm** topology because the values of $r_{m/n}$ are far from 1.37. Indeed, the second and third monomers experimentally led to the formation of COFs with **bex** topology,[52,56] an edge-transitive net for which only angle matching is required.[16] In the case of the combination of TAPP and BATA, the $r_{m/n}$ is 1.56, which is close to the theoretical value of 1.37. As a result, a COF with **mcm** topology can be expected from their condensation under suitable conditions.

To elucidate the crystal structures of the as-synthesized polymers, theoretical PXRD patterns of the COFs with both **bex** and **mcm** nets were simulated and compared with the experimentally observed PXRD data. As shown in Fig. 2a, although the two structures with different topologies display similar theoretical PXRD patterns, a noticeable difference can still be identified at the position of $2\theta = 5.46°$, where the **mcm** structure has a clear diffraction peak but such a peak is absent for the **bex** structure. The experimental PXRD pattern collected for COF-BATA-TAPP-Zn displays an intense peak at 4.87° (200 facet). Notably, a peak was observed at 5.46°, which corresponds to the (210) facet of the COF with **mcm** topology, strongly suggesting that the as-obtained COF possesses a **mcm** net. In addition, diffraction peaks were also observed at 2.50°, 3.48°,

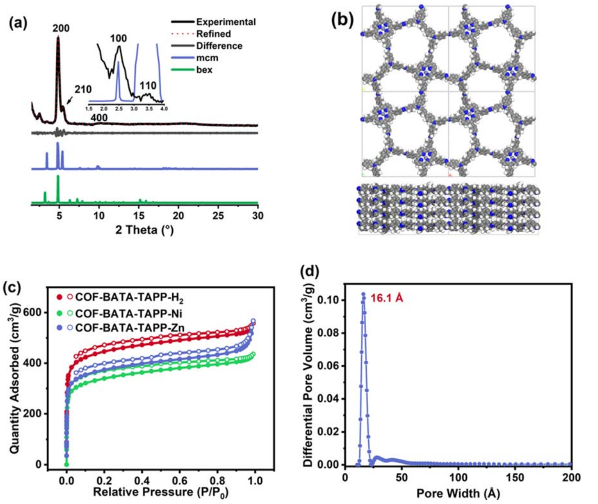

Fig. 2 (a) Experimental (black) and Pawley refined (red) PXRD patterns, and their difference (gray), and simulated PXRD patterns for BATA-TAPP-Zn with the **mcm** net (blue) and **bex** net (green). (b) Lattice structure of BATA-TAPP-Zn from top and side views (gray, carbon and zinc; blue, nitrogen; white, hydrogen). (c) Nitrogen adsorption–desorption isotherms of the three COFs. (d) Pore size distribution profile of COF-BATA-TAPP-Zn.

and 9.85°, which are assigned to (100), (110), and (400) facets, respectively. Pawley refinement performed on its experimental PXRD pattern against an eclipsed stacking model (Fig. 2b) afforded unit cell parameters of $a = 37.60$ Å, $b = 37.17$ Å, $c = 4.91$ Å, and $\alpha = \beta = \gamma = 90°$ ($R_{\text{wp}} = 5.40\%$ and $R_{\text{p}} = 4.12\%$). COF-BATA-TAPP-H_2 and COF-BATA-TAPP-Ni displayed PXRD patterns similar to that of COF-BATA-TAPP-Zn. Although their (210) peaks are weak, they could still be identified (Fig. S12 and S13†), suggesting that they also hold a **mcm** net. The cell parameters of COF-BATA-TAPP-H_2 and BATA-TAPP-Ni were also obtained by Pawley refinement, which are $a = 37.70$ Å, $b = 37.96$ Å, $c = 4.22$ Å, and $\alpha = \beta = \gamma = 90°$ ($R_{\text{wp}} = 4.65\%$ and $R_{\text{p}} = 3.65\%$) for the former, and $a = 37.66$ Å, $b = 37.43$ Å, $c = 4.95$ Å, and $\alpha = \beta = \gamma = 90°$ ($R_{\text{wp}} = 4.08\%$ and $R_{\text{p}} = 3.15\%$) for the latter, respectively.

Another piece of evidence for the formation of the COFs with **mcm** topology was provided by experimental results from nitrogen adsorption–desorption measurements. As shown in Fig. 2c, all of the three COFs displayed typical type-I sorption isotherms and steep nitrogen uptakes in the low-pressure range ($P/P_0 = 0$–0.01), indicating a permanent microporous feature. Brunauer–Emmett–Teller (BET) surface areas were calculated to be 1696, 1280, and 1417 $m^2 g^{-1}$ for COF-BATA-TAPP-H_2, COF-BATA-TAPP-Ni, and COF-BATA-TAPP-Zn, respectively (Fig. S14†). Pore size distributions calculated based on the quenched solid density functional theory (QSDFT) method showed narrow distributions at 16.1 Å (COF-BATA-TAPP-Zn), 16.7 Å (COF-BATA-TAPP-H_2), and 16.1 Å (COF-BATA-TAPP-Ni) (Fig. 2d and S15†). These values agree well with the theoretical pore sizes of the COFs with **mcm** topology (15.0 Å, Scheme 1), but are different from that predicted for the COFs with **bex** topology, which possess two different kinds of pores with apertures of 10.2 and 16.6 Å (Fig. S16†).

The orderly arranged porphyrin arrays in the crystalline frameworks might endow them with excellent photocatalytic activity. Thus the potential of the three COFs as photocatalysts was investigated. For this purpose, their optical and electronic properties were studied first. Their ultraviolet-visible (UV-vis) diffuse reflectance spectra show that light across the UV to visible spectrum could be absorbed by the COFs, with absorption edges ranging from 600 to 700 nm (Fig. 3a). The optical band gaps of COF-BATA-TAPP-H_2, COF-BATA-TAPP-Ni, and COF-BATA-TAPP-Zn were calculated to be 1.79, 1.91, and 1.87 eV, respectively, based on the corresponding Tauc plots (Fig. S17†). The narrow range of these values (1.79–1.91 eV) suggests that the optical band gaps of these COFs are not significantly influenced by the different metalation of the porphyrin unit. The Mott–Schottky plots reveal that the three COFs are n-type semiconductors and their flat band potentials were calculated to be −1.38, −1.40, and −1.17 V (*vs.* Ag/AgCl) for COF-BATA-TAPP-H_2, COF-BATA-TAPP-Ni, and COF-BATA-TAPP-Zn, respectively (Fig. 3b–d). An energy level diagram is presented in Fig. 3e. The lowest unoccupied molecular orbital (LUMO) energy levels were calculated to be approximately −3.28 to −3.49 eV, higher than the potential of the HER, indicating that these COFs have the potential for the photocatalytic HER from water. In addition, the valence band XPS analysis of the three COFs gave similar results (Fig. S18 and Table S2†).

To further investigate the carrier separation and migration behaviour of the three COFs, photoelectrochemical measurements were performed. According to the results obtained from electrochemical impedance spectroscopy (EIS, Fig. S19†), COF-BATA-TAPP-Zn has the smallest arc radius among the three COFs, indicating the lowest charge-transfer resistance. The arc radius of all three COFs decreases after irradiation, which is attributed to the generation of photoinduced charge carriers. From the results of the linear sweep voltammetry (LSV) experiment (Fig. S20†), COF-BATA-TAPP-Zn displays a much higher current density than the other two COFs in the dark and under visible-light. The current density of all three COFs is enhanced after light irradiation, which is concordant with the EIS results. Photocurrent tests were further conducted for all three COFs to evaluate their photoelectric responses. The experimental results show that the photoelectric responses display an order of COF-BATA-TAPP-Zn > COF-BATA-TAPP-Ni > COF-BATA-TAPP-H_2 (Fig. 3f). Besides that, the intensity enhancement of the signals in the electron paramagnetic resonance (EPR) spectra of COF-BATA-TAPP-H_2 and COF-BATA-TAPP-Zn under light also indicated the generation of photoinduced charge carriers (Fig. S21 and S22†). These outcomes suggest that the introduction of metal ions into the porphyrin unit improves the charge carrier transport ability of the COFs, with COF-BATA-TAPP-Zn displaying the most efficient charge carrier transport.

The photocatalytic performance of the three COFs was evaluated for hydrogen evolution from water under a visible-light source (Xe-lamp 300 W, $\lambda > 400$ nm) in the presence of ascorbate acid and H_2PtCl_6, with ascorbate acid employed as a sacrificial reagent and H_2PtCl_6 serving as a precursor of the co-

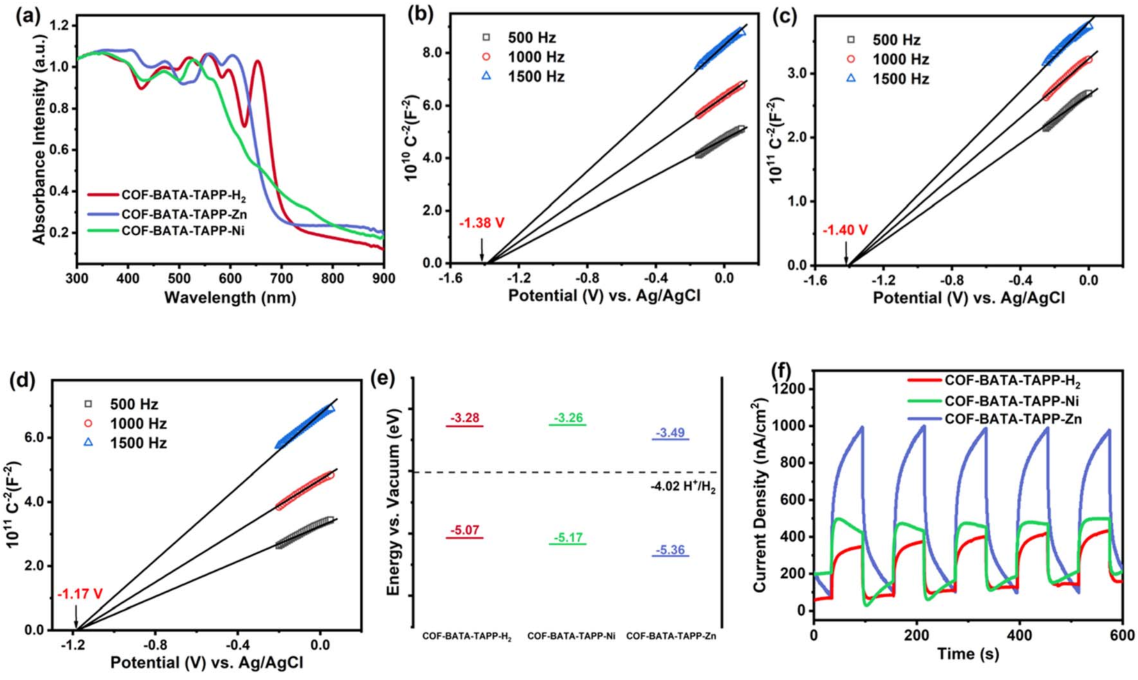

Fig. 3 (a) UV-vis adsorption spectra of COF-BATA-TAPP-H_2 (red), COF-BATA-TAPP-Ni (green), and COF-BATA-TAPP-Zn (blue). Mott–Schottky plots of (b) COF-BATA-TAPP-H_2, (c) COF-BATA-TAPP-Ni, and (d) COF-BATA-TAPP-Zn. (e) Comparison of the frontier orbital energies of the COFs and the redox potential of water. (f) Photocurrent of COF-BATA-TAPP-H_2 (red), COF-BATA-TAPP-Ni (green), and COF-BATA-TAPP-Zn (blue).

catalyst. Because of its best photocurrent performance, COF-BATA-TAPP-Zn was selected for optimizing the conditions for photocatalytic H_2 evolution. A certain amount of Pt, which facilitated the dissociation of photogenerated exciton and proton coupling, was *in situ* photodeposited on the COF surface during the reaction. It was found that the H_2 evolution rate of COF-BATA-TAPP-Zn was significantly influenced by the amount of Pt (Fig. S23†). When Pt was absent as the co-catalyst, no obvious H_2 evolution was detected by gas chromatography. With the amount of Pt was increased from 0 to 0.76 wt%, the H_2 evolution rate of the COF gradually rose to 10.0 mmol g^{-1} h^{-1}. However, upon further increasing the amount of Pt to 5.71 wt%, the H_2 evolution rate of COF-BATA-TAPP-Zn dropped to 3.3 mmol g^{-1} h^{-1}. Such a reduction in the H_2 evolution rate was attributed to the excessive Pt loading, which would hinder light absorption and often serve as a major site for charge-carrier recombination.[62] The content of deposited Pt on COF-BATA-TAPP-Zn was optimized to be 0.76 wt% to achieve a maximum H_2 evolution rate. Subsequently, the H_2 evolution performance of the other two COFs was measured under the same conditions. The trend in H_2 evolution performance was observed as COF-BATA-TAPP-Zn (10.0 mmol g^{-1} h^{-1}) > COF-BATA-TAPP-Ni (3.2 mmol g^{-1} h^{-1}) > COF-BATA-TAPP-H_2 (1.7 mmol g^{-1} h^{-1}) (Fig. 4a), consistent with the results of the photoelectric response experiment. Compared with other COF and POP-based HER photocatalysts previously reported, COF-BATA-TAPP-Zn displayed a good HER ability with a low amount of Pt co-catalyst (Table S3†). Furthermore, the photocatalytic stability of COF-BATA-TAPP-Zn was evaluated by adding a certain amount of ascorbic acid into the reaction system every 4 hours. It was observed that the reaction system maintained robust durability in photocatalytic hydrogen evolution over the course of five recycle experiments (Fig. 4b), indicating that the COF exhibited good photocatalytic stability. Moreover, a comparison of the FT-IR spectra of COF-BATA-TAPP-Zn before and after the photocatalytic reaction showed no obvious difference, indicating structural integration of the COF during photocatalysis (Fig. S24†).

In these COFs, the eclipsed interlayer stacking results in well-ordered porphyrin columns, forming macrocycle-on-macrocycle and metal-on-metal channels, which play pivotal roles in charge carrier separation and migration. In the case of COF-BATA-TAPP-Zn, holes could readily migrate *via* the macrocycle-on-macrocycle channel to the surface of the COF, while electrons could transfer *via* the Zn⋯Zn chain.[63] In COF-BATA-TAPP-Ni, the decrease of d-electrons in the central metal-ion ($3d^8$ for Ni^{2+}) introduces the possibility of the ligand-

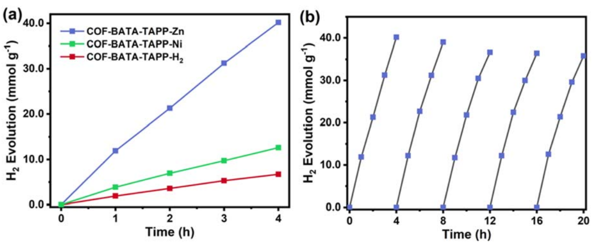

Fig. 4 (a) Time course for photocatalytic H_2 production under visible irradiation for COF-BATA-TAPP-H_2 (red), COF-BATA-TAPP-Ni (green), and COF-BATA-TAPP-Zn (blue). (b) Photocatalytic H_2 production with COF-BATA-TAPP-Zn in five recycles.

to-metal charge transfer (LMCT) process, which would restrain hole migration *via* the macrocycle-on-macrocycle channel. This increases the possibility of charge recombination. For COF-BATA-TAPP-H_2, photogenerated electron and hole migration would proceed solely *via* the macrocycle-on-macrocycle pathway due to the absence of metal ions, leading to the highest probability of charge recombination.[63] Therefore, COF-BATA-TAPP-Zn displayed a much higher H_2 evolution ability than COF-BATA-TAPP-Ni and COF-BATA-TAPP-H_2. Additionally, TEM analysis showed that Pt nanoparticles (NPs) *in situ* formed with the COFs under light irradiation. Remarkably, COF-BATA-TAPP-Zn displayed a significantly higher abundance of Pt NPs, with an average size of about 1.5 nm. This size is notably smaller than the average size of Pt NPs observed for COF-BATA-TAPP-H_2 and COF-BATA-TAPP-Ni (about 3 nm, Fig. S25–27†). The superior H_2 evolution ability of COF-BATA-TAPP-Zn over the other two COFs could partly be attributed to the co-existence of the uniform dispersion of Pt NPs.

Conclusions

In summary, **mcm** topology, whose structure is solely tiled by pentagons, has been identified for COFs for the first time. Three COFs were constructed through imine condensation reactions of a porphyrin-based tetraamines and a D_{2h} symmetric tetraaldehyde. It is the matched angle and length of the building blocks that lead to the formation of the 2D COFs with a **mcm** net. The COFs comprise only pentagonal pores, which is a new shape complement to the COFs with homogeneous porosity, which mainly comprise triangular, quadrilateral, or hexagonal pores. Thanks to the well-ordered arrays of the porphyrin units in the COFs and the conjugated 2D frameworks, the COFs exhibit impressive photocatalytic ability for hydrogen evolution from water, with the highest hydrogen evolution rate up to 10.0 mmol g^{-1} h^{-1}. These findings not only increase the diversity of the topological structure of COFs, but also underscore the significance of structural design for COFs with targeted topology and function, which should be instructive for the development of novel and high-performance crystalline porous materials.

Data availability

The data have been provided in ESI.†

Author contributions

X. Z., P. T. and X. H. conceived and designed the experiments. P. T. and X. H. performed the experiments. Q. Q. aided in the structural simulations. X. Z. and P. T. wrote the manuscript. X. Z. directed the research.

Conflicts of interest

There are no conflicts to declare.

Acknowledgements

We thank the National Natural Science Foundation of China (No. 21632004) and State Key Laboratory of Advanced Technology for Materials Synthesis and Processing (Wuhan University of Technology) for financial support (2023-KF-6). We would like to thank Professor Shengqiang Xiao (Wuhan University of Technology) for assisting with the PXRD measurements.

Notes and references

1 S. Kandambeth, K. Dey and R. Banerjee, *J. Am. Chem. Soc.*, 2019, **141**, 1807–1822.
2 K. Geng, T. He, R. Liu, S. Dalapati, K. T. Tan, Z. Li, S. Tao, Y. Gong, Q. Jiang and D. Jiang, *Chem. Rev.*, 2020, **120**, 8814–8933.
3 R.-R. Liang, S.-Y. Jiang, R.-H. A and X. Zhao, *Chem. Soc. Rev.*, 2020, **49**, 3920–3951.
4 B. Gui, H. Ding, Y. Cheng, A. Mal and C. Wang, *Trends Chem.*, 2022, **4**, 437–450.
5 A. M. Evans, M. J. Strauss, A. R. Corcos, Z. Hirani, W. Ji, L. S. Hamachi, X. Aguilar-Enriquez, A. D. Chavez, B. J. Smith and W. R. Dichtel, *Chem. Rev.*, 2022, **122**, 442–564.
6 X. Guan, F. Chen, Q. Fang and S. Qiu, *Chem. Soc. Rev.*, 2020, **49**, 1357–1384.
7 Please note that a few one-dimensional (1D) COFs have also been reported recently. For examples, please see: C. Jia, A. Duan, C. Liu, W.-Z. Wang, S.-X. Gan, Q.-Y. Qi, Y. Li, X. Huang and X. Zhao, *Small*, 2023, **19**, 2300518, and the references therein.
8 W. Liu, K. Wang, X. Zhan, Z. Liu, X. Yang, Y. Jin, B. Yu, L. Gong, H. Wang, D. Qi, D. Yuan and J. Jiang, *J. Am. Chem. Soc.*, 2023, **145**, 8141–8149.
9 X. Guan, F. Chen, S. Qiu and Q. Fang, *Angew. Chem., Int. Ed.*, 2023, **62**, e202213203.
10 L. Liao, X. Guan, H. Zheng, Z. Zhang, Y. Liu, H. Li, L. Zhu, S. Qiu, X. Yao and Q. Fang, *Chem. Sci.*, 2022, **13**, 9305–9309.
11 A. P. Côté, A. I. Benin, N. W. Ockwig, M. O'Keeffe, A. J. Matzger and O. M. Yaghi, *Science*, 2005, **310**, 1166–1170.
12 S. Dalapati, M. Addicoat, S. Jin, T. Sakurai, J. Gao, H. Xu, S. Irle, S. Seki and D. Jiang, *Nat. Commun.*, 2015, **6**, 7786.
13 E. L. Spitler and W. R. Dichtel, *Nat. Chem.*, 2010, **2**, 672–677.
14 T.-Y. Zhou, S.-Q. Xu, Q. Wen, Z.-F. Pang and X. Zhao, *J. Am. Chem. Soc.*, 2014, **136**, 15885–15888.
15 S.-Q. Xu, R.-R. Liang, T.-G. Zhan, Q.-Y. Qi and X. Zhao, *Chem. Commun.*, 2017, **53**, 2431–2434.
16 B. Zhang, H. Mao, R. Matheu, J. A. Reimer, S. A. Alshmimri, S. Alshihri and O. M. Yaghi, *J. Am. Chem. Soc.*, 2019, **141**, 11420–11424.
17 H. L. Nguyen, N. Hanikel, S. J. Lyle, C. Zhu, D. M. Proserpio and O. M. Yaghi, *J. Am. Chem. Soc.*, 2020, **142**, 2218–2221.
18 T. Banerjee, F. Haase, S. Trenker, B. P. Biswal, G. Savasci, V. Duppel, I. Moudrakovski, C. Ochsenfeld and B. V. Lotsch, *Nat. Commun.*, 2019, **10**, 2689.
19 C. Qian, Q.-Y. Qi, G.-F. Jiang, F.-Z. Cui, Y. Tian and X. Zhao, *J. Am. Chem. Soc.*, 2017, **139**, 6736–6743.

20 S.-Y. Jiang, S.-X. Gan, X. Zhang, H. Li, Q.-Y. Qi, F.-Z. Cui, J. Lu and X. Zhao, *J. Am. Chem. Soc.*, 2019, **141**, 14981–14986.

21 S.-L. Cai, Z.-H. He, X.-L. Li, K. Zhang, S.-R. Zheng, J. Fan, Y. Liu and W.-G. Zhang, *Chem. Commun.*, 2019, **55**, 13454–13457.

22 X. Wang, X. Han, C. Cheng, X. Kang, Y. Liu and Y. Cui, *J. Am. Chem. Soc.*, 2022, **144**, 7366–7373.

23 Z. Yang, W. Hao, X. Su, T. Zhang, W. Chen, G. Zhang and L. Chen, *Chem. Mater.*, 2022, **34**, 5888–5895.

24 Y. Lan, X. Han, M. Tong, H. Huang, Q. Yang, D. Liu, X. Zhao and C. Zhong, *Nat. Commun.*, 2018, **9**, 5274.

25 H. Q. Pham and N.-N. Pham-Tran, *Chem. Mater.*, 2021, **33**, 4488–4499.

26 Y. Zeng, R. Zou and Y. Zhao, *Adv. Mater.*, 2016, **28**, 2855–2873.

27 J. Fu, S. Das, G. Xing, T. Ben, V. Valtchev and S. Qiu, *J. Am. Chem. Soc.*, 2016, **138**, 7673–7680.

28 C. J. Doonan, D. J. Tranchemontagne, T. G. Glover, J. R. Hunt and O. M. Yaghi, *Nat. Chem.*, 2010, **2**, 235–238.

29 Q. Gao, L. Bai, X. Zhang, P. Wang, P. Li, Y. Zeng, R. Zou and Y. Zhao, *Chin. J. Chem.*, 2015, **33**, 90–94.

30 L. Liu, Y. Hu, S. Huang, Y. Jin, J. Cui, W. Gong and W. Zhang, *Chem. Sci.*, 2021, **12**, 13316–13320.

31 X. Han, Q. Xia, J. Huang, Y. Liu, C. Tan and Y. Cui, *J. Am. Chem. Soc.*, 2017, **139**, 8693–8697.

32 Z. Fu, C. Shu, X. Wang, L. Chen, X. Wang, L. Liu, K. Wang, R. Clowes, S. Y. Chong, X. Wu and A. I. Cooper, *CCS Chem.*, 2023, **5**, 2290–2300.

33 W. Wang, H. Wang, X. Tang, J. Huo, Y. Su, C. Lu, Y. Zhang, H. Xu and C. Gu, *Chem. Sci.*, 2022, **13**, 8679–8685.

34 M. Dogru, M. Handloser, F. Auras, T. Kunz, D. Medina, A. Hartschuh, P. Knochel and T. Bein, *Angew. Chem., Int. Ed.*, 2013, **52**, 2920–2924.

35 Y. Du, H. Yang, J. M. Whiteley, S. Wan, Y. Jin, S. H. Lee and W. Zhang, *Angew. Chem., Int. Ed.*, 2016, **55**, 1737–1741.

36 S. Wan, J. Guo, J. Kim, H. Ihee and D. Jiang, *Angew. Chem., Int. Ed.*, 2008, **47**, 8826–8830.

37 S. Wang, Q. Wang, P. Shao, Y. Han, X. Gao, L. Ma, S. Yuan, X. Ma, J. Zhou, X. Feng and B. Wang, *J. Am. Chem. Soc.*, 2017, **139**, 4258–4261.

38 S. Dalapati, S. Jin, J. Gao, Y. Xu, A. Nagai and D. Jiang, *J. Am. Chem. Soc.*, 2013, **135**, 17310–17313.

39 S.-Y. Ding, M. Dong, Y.-W. Wang, Y.-T. Chen, H.-Z. Wang, C.-Y. Su and W. Wang, *J. Am. Chem. Soc.*, 2016, **138**, 3031–3037.

40 N. Huang, X. Ding, J. Kim, H. Ihee and D. Jiang, *Angew. Chem., Int. Ed.*, 2015, **54**, 8704–8707.

41 M. Dogru and T. Bein, *Chem. Commun.*, 2014, **50**, 5531–5546.

42 R. Li, G. Xing, H. Li, S. Li and L. Chen, *Chin. Chem. Lett.*, 2023, **34**, 107454.

43 D. W. Burke, R. R. Dasari, V. K. Sangwan, A. K. Oanta, Z. Hirani, C. E. Pelkowski, Y. Tang, R. Li, D. C. Ralph, M. C. Hersam, S. Barlow, S. R. Marder and W. R. Dichtel, *J. Am. Chem. Soc.*, 2023, **145**, 11969–11977.

44 L. Dai, A. Dong, X. Meng, H. Liu, Y. Li, P. Li and B. Wang, *Angew. Chem., Int. Ed.*, 2023, **62**, e202300224.

45 L. Stegbauer, K. Schwinghammer and B. V. Lotsch, *Chem. Sci.*, 2014, **5**, 2789–2793.

46 L. Sun, M. Lu, Z. Yang, Z. Yu, X. Su, Y. Q. Lan and L. Chen, *Angew. Chem., Int. Ed.*, 2022, **61**, e202204326.

47 R. Shen, C. Qin, L. Hao, X. Li, P. Zhang and X. Li, *Adv. Mater.*, 2023, **35**, 2305397.

48 T. Zhou, L. Wang, X. Huang, J. Unruangsri, H. Zhang, R. Wang, Q. Song, Q. Yang, W. Li, C. Wang, K. Takahashi, H. Xu and J. Guo, *Nat. Commun.*, 2021, **12**, 3934.

49 Y. Li, G. Cui, X. Cai, G. Yun, Y. Zhao, L. Jiang, S. Cui, J. Zhang, M. Liu, W. Zeng, Z. Wang and J. Jiang, *Chem.–Eur. J.*, 2024, **30**, e202303688.

50 A. Chatterjee, J. Sun, K. S. Rawat, V. Van Speybroeck and P. Van Der Voort, *Small*, 2023, **19**, 2303189.

51 L. Zhang, Y. Xiao, Q.-C. Yang, L.-L. Yang, S.-C. Wan, S. Wang, L. Zhang, H. Deng and Z.-J. Sun, *Adv. Funct. Mater.*, 2022, **32**, 2201542.

52 L. Gong, X. Yang, Y. Gao, G. Yang, Z. Yu, X. Fu, Y. Wang, D. Qi, Y. Bian, K. Wang and J. Jiang, *J. Mater. Chem. A*, 2022, **10**, 16595–16601.

53 J.-Y. Yue, Y.-T. Wang, X. Wu, P. Yang, Y. Ma, X.-H. Liu and B. Tang, *Chem. Commun.*, 2021, **57**, 12619–12622.

54 Q. Wu, R.-K. Xie, M.-J. Mao, G.-L. Chai, J.-D. Yi, S.-S. Zhao, Y.-B. Huang and R. Cao, *ACS Energy Lett.*, 2020, **5**, 1005–1012.

55 H. Lv, R. Sa, P. Li, D. Yuan, X. Wang and R. Wang, *Sci. China: Chem.*, 2020, **63**, 1289–1294.

56 S. Bhunia, S. K. Das, R. Jana, S. C. Peter, S. Bhattacharya, M. Addicoat, A. Bhaumik and A. Pradhan, *ACS Appl. Mater. Interfaces*, 2017, **9**, 23843–23851.

57 H. He, X. Fang, D. Zhai, W. Zhou, Y. Li, W. Zhao, C. Liu, Z. Li and W. Deng, *Chem.–Eur. J.*, 2021, **27**, 14390–14395.

58 S. An, C. Lu, Q. Xu, C. Lian, C. Peng, J. Hu, X. Zhuang and H. Liu, *ACS Energy Lett.*, 2021, **6**, 3496–3502.

59 Please note that some of the structures reported in ref. 49–58 look like a sql net, especially when the length of building block II is short. For example, please see ref. 55 and 57.

60 M. Liu, S. Liu, C. X. Cui, Q. Miao, Y. He, X. Li, Q. Xu and G. Zeng, *Angew. Chem., Int. Ed.*, 2022, **61**, e202213522.

61 Y. Zhu, D. Zhu, Y. Chen, Q. Yan, C. Y. Liu, K. Ling, Y. Liu, D. Lee, X. Wu, T. P. Senftle and R. Verduzco, *Chem. Sci.*, 2021, **12**, 16092–16099.

62 J. B. Sambur, T. Y. Chen, E. Choudhary, G. Chen, E. J. Nissen, E. M. Thomas, N. Zou and P. Chen, *Nature*, 2016, **530**, 77–80.

63 R. Chen, Y. Wang, Y. Ma, A. Mal, X. Y. Gao, L. Gao, L. Qiao, X. B. Li, L. Z. Wu and C. Wang, *Nat. Commun.*, 2021, **12**, 1354.